







# Long transit time from the Seafloor to the Ice Shell on Enceladus

Yixiao Zhang <sup>1</sup>★, Suyash Bire <sup>1,2</sup>, Shuang Wang <sup>1</sup>, Anika Nath,<sup>1</sup> Ali Ramadhan <sup>1</sup>, Wanying Kang <sup>1</sup>  
and John Marshall <sup>1</sup>

<sup>1</sup>*Earth, Atmospheric, and Planetary Sciences, Massachusetts Institute of Technology, Cambridge, MA 02139, US*

<sup>2</sup>*Centre for Climate Studies, Indian Institute of Technology Bombay, Powai, Mumbai, Maharashtra 400076, India*

Accepted 2025 June 11. Received 2025 June 10; in original form 2025 February 24

## ABSTRACT

Tidal heating within the rocky core of Enceladus can drive convection in the ocean, inducing material transfer between the sea floor and the ice shell. This heating may be focused into narrow stripes, enhancing local heating rates that could trigger convection. Here, we use high-resolution numerical simulations to investigate the transport of tracers from the seafloor to the ocean top due to convection initiated by bottom heating patterns. For parameters typical of Enceladus, we find that horizontal temperature gradients induced by uneven bottom heating patterns generate turbulent vortices due to baroclinic instability. The resulting lateral mixing makes plumes spread horizontally quickly by entraining the cold ambient water, possibly mixing away lateral temperature gradients by the time the plume reaches the ocean top. The natural Rossby number, a non-dimensional number that characterizes the importance of rotation, is identified as a controlling parameter. Small natural Rossby numbers correspond to rotationally dominated plumes, vigorous lateral mixing, and slow vertical transport. Large natural Rossby numbers correspond to non-rotating plumes that rapidly bring tracers to the ocean top with limited lateral spreading. We establish a scaling between the vertical transit time and the natural Rossby number, which predicts a transit time of tens of years or more across the ocean of Enceladus. This long transit time is inconsistent with an association between silicon-rich particles in the E ring of Saturn and hydrothermal activity on Enceladus transporting silica particles from the core to the surface. Finally, a detailed regime diagram is presented to summarize our results.

**Key words:** Methods: numerical – Planets and Satellites: Oceans.

## 1 INTRODUCTION

The ocean (Iess et al. 2014; Thomas et al. 2016) beneath the Enceladus ice shell makes it a compelling target for life searching beyond the earth. The heat used to sustain the ocean originates from tidal dissipation in the ice shell or the silicate core, as Enceladus revolves around Saturn in an elliptical orbit (Beuthe 2016, 2018, 2019; Choblet et al. 2017). This heat production is concentrated toward the south polar region of Enceladus, keeping the polar ice shell thinner than elsewhere, which then leads to formation of active geysers that features high surface temperature and vigorous outgoing energy flux (Porco et al. 2006; Abramov & Spencer 2009; Čadež et al. 2016; Tajeddine et al. 2017; Hemingway & Mittal 2019; McKinnon & Schenk 2021). The geysers there continuously eject materials from the interior of Enceladus into space. In the ejecta, various constituents have been detected, including water, sodium salt, carbon dioxide, simple organic compounds, and silica particles (Waite et al. 2006; Postberg et al. 2009, 2018; Taubner et al. 2018). Hydrothermal activity has been hypothesized to occur on the seafloor of Enceladus, to generate detected silica particles (Hsu et al. 2015). Since particles grow in a saturated solution, an upper bound of several weeks/months can be placed on the transit time from the seafloor to

the ice shell, based on the observed particle size (Hsu et al. 2015). Transit times deduced from a consideration of fluid mechanics range from several weeks, based on free-fall scaling (Sekine et al. 2015; Choblet et al. 2017; Schoenfeld et al. 2023), to hundreds of years or beyond, based on timescales for diffusive processes or rotating convection (Zeng & Jansen 2021; Kang et al. 2022; Bire et al. 2023). To narrow uncertainties, it is crucial to understand the nature of fluid motion triggered by purported concentrated heat sources on the seafloor (Choblet et al. 2017).

Attempts to estimate transit time due to hydrothermal sources were begun with Europa, an icy moon of Jupiter. Using both numerical simulations and laboratory experiments, convective plumes on Europa have been shown to remain concentrated as they penetrate up from the seafloor to the ice shell. In Europa’s parameter regime, the dilution is inhibited by a rim current that develops around the plumes (Collins et al. 2000; Thomson & Delaney 2001; Goodman et al. 2004; Vance & Goodman 2009; Goodman & Lenferink 2012; Soderlund et al. 2014). The transit time is estimated to be around 15–20 d for hydrothermal plumes energized by localized heat fluxes of 10 GW, initiating a single giant plume; see Vance & Goodman (2009), whose peak is of the order of  $10 \sim 100 \text{ W m}^{-2}$  (Goodman et al. 2004; Goodman & Lenferink 2012). On Enceladus, the heat source is estimated to be rather weaker (peak at  $10 \text{ W m}^{-2}$ ; Choblet et al. 2017). Taking into account that gravity is ten times weaker, the thermal expansion coefficient is smaller due to low salinity and lower

\* E-mail: [yixiaoz@mit.edu](mailto:yixiaoz@mit.edu)

pressure, the buoyancy forcing at the seafloor of Enceladus is likely two orders of magnitude weaker than on Europa. At this forcing level, plume instability might be expected and has been reported (Bush & Woods 1999; Kang et al. 2022; Bire et al. 2023). As plumes become unstable and scatter horizontally, one may expect the vertical tracer transport to slow down and the tracer concentration to decrease (Zeng & Jansen 2021; Kang et al. 2022; Bire et al. 2023).

The goal of this study is to answer two related questions: (1) Do plumes emanating from the sea floor on Enceladus remain concentrated until they impact the ice shell? (2) How long does it take for them to transport tracers from the seafloor to the ice? Motivated by Choblet et al. (2017), we consider a heat source concentrated along a straight line. During the early stage of plume development, cold ambient water is entrained into the rising plume. At a sufficiently large distance from the source, the original heat source can be idealized as either a point or a line source (Turner 1969; Bush & Woods 1999). The dynamics of a line plume are governed by the integrated heat flux,  $Q^{(\text{line})}$ , across the line source, with units of  $\text{W m}^{-1}$ . This quantity determines the amount of heat injected into the system per unit length, which in turn is distributed to the entrained ambient fluid. Combining  $Q^{(\text{line})}$ , the planetary rotation rate  $\Omega$  and the ocean depth  $H$ , we obtain the natural Rossby number that governs the dynamics of a line plume,

$$\text{Ro}^{*(\text{line})} = \frac{1}{H} \left( \frac{B^{(\text{line})}}{(2\Omega)^3} \right)^{\frac{1}{3}}, \quad (1)$$

where  $B^{(\text{line})}$  is the buoyancy flux integrated across the line source ( $B^{(\text{line})} = \alpha g Q^{(\text{line})} / \rho_0 c_p$ , where  $\alpha$ ,  $\rho_0$ , and  $c_p$  is the thermal expansion coefficient, density, and specific heat capacity of seawater, respectively). This non-dimensional number captures the ratio between the rotational length scale (Jones & Marshall 1993) and the ocean depth  $H$ , and determines whether the plume will remain concentrated or, due to its instability, spread laterally.

After the plume destabilizes and spreads laterally (Bush & Woods 1999; Kang et al. 2022; Bire et al. 2023), the upward heat flux becomes horizontally homogenized and the information regarding the heating pattern is completely lost, so that the area-averaged heat flux  $Q^{(\text{area})}$  (in units of  $\text{W m}^{-2}$ ) replaces  $Q^{(\text{line})}$  in governing the subsequent evolution. In this regime, the dynamics is governed by the area-averaged Rossby number,

$$\text{Ro}^{*(\text{area})} = \frac{1}{H} \left( \frac{B^{(\text{area})}}{(2\Omega)^3} \right)^{\frac{1}{2}}, \quad (2)$$

where  $B^{(\text{area})}$  is the average buoyancy flux prescribed at the bottom ( $B^{(\text{area})} = \alpha g Q^{(\text{area})} / \rho_0 c_p$ ).  $\text{Ro}^{*(\text{area})}$  is identical to the natural Rossby number introduced in oceanography in the 1990s (Jones & Marshall 1993; Maxworthy & Narimousa 1994), as the ratio between a rotational length scale and the depth of the ocean. We also note that  $\text{Ro}^{*(\text{area})}$  is the square root of the modified flux Rayleigh number ( $\text{Ra}_F^* = B^{(\text{area})} / (2\Omega)^3 H^2$ ) commonly used in rotating Rayleigh-Bénard convection (Christensen & Aubert 2006; Aurnou, Horn & Julien 2020). This non-dimensional number describes how many rotation periods it takes for the array of rotation-governed helical plumes to penetrate the ocean depth (Fernando, Chen & Boyer 1991; Jones & Marshall 1993; Maxworthy & Narimousa 1994; Aurnou et al. 2003; Aurnou et al. 2020; Bire et al. 2022, 2023). For Enceladus, since the total heat production is on average  $Q^{(\text{area})} = 0.04 \text{ W m}^{-2}$  over the globe (Sekine et al. 2015; Choblet et al. 2017; Hemingway & Mittal 2019; Ermakov et al. 2021; Nimmo, Neveu & Howett 2023),  $\text{Ro}^{*(\text{area})}$  is subject to an upper bound of  $2 \times 10^{-6}$ , assuming  $\alpha = 1 \times 10^{-5} \text{ K}^{-1}$ ,  $\rho_0 = 1.02 \times 10^3 \text{ kg m}^{-3}$ ,  $c_p = 4 \times 10^3 \text{ J kg}^{-1} \text{ K}^{-1}$  (Soder-

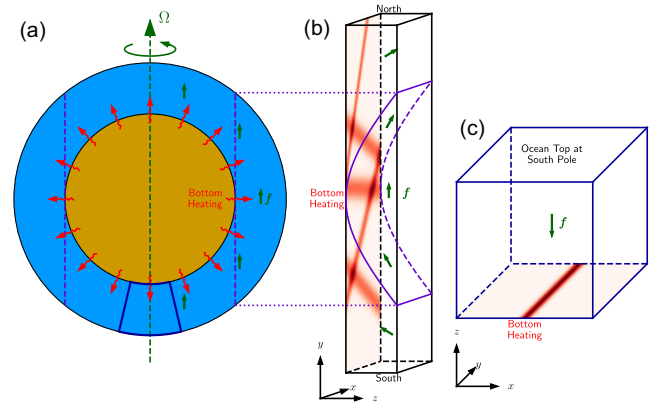


**Figure 1.** Schema showing the setup of our numerical simulation. Panel (A) is a diagram of Enceladus, the ocean of which is treated as a spherical shell. Ocean circulation is driven by bottom heating (red curved arrows) and modulated by the rotation of the moon (represented by the green arrows shown on the right side). The dashed purple lines mark the tangent cylinder. The blue box at the South Pole represents the domain of our regional simulations and is depicted in Panel (C) in better detail. Panel (B) shows the setup of our near-global simulation. The domain is a Cartesian box:  $x$  and  $y$  directions represent east and north, respectively, and the domain extends from the South Pole to the North Pole latitudinally. The bottom heating is focused into stripes (marked red in Panel B) in analogy to Choblet et al. (2017).  $\mathbf{f}$  includes both the traditional and non-traditional components of the Coriolis acceleration and varies with latitude. The purple curve marks the tangent cylinder that follows  $\mathbf{f}$  locally: the dotted lines connect the tangent cylinder in spherical geometry (Panel A) to that in Cartesian geometry (Panel B). Panel (C) is a schema of our regional simulation. The domain is a  $20 \text{ km} \times 20 \text{ km} \times 20 \text{ km}$  box. The bottom heating is focused over a single strip, and  $\mathbf{f} = -2\Omega\hat{\mathbf{z}}$  everywhere. Panels (A) and (B) are adapted from fig. 1 of Bire et al. (2022).

lund 2019),  $\Omega = 5.3 \times 10^{-5} \text{ s}^{-1}$ ,  $g = 0.1 \text{ m s}^{-2}$  and  $H = 40 \text{ km}$  (Čadek et al. 2016; Tajeddine et al. 2017; Hemingway & Mittal 2019; McKinnon & Schenk 2021).  $\text{Ro}^{*(\text{area})}$  puts a strong constraint on the behaviour of convective plumes in the ocean of Enceladus and will be the key to connecting numerical simulations, laboratory experiments, and realistic icy moons.

Our paper is organized as follows: We describe our model design and how we diagnose the transit time in Section 2; the phenomena of the reference simulations for rotating line plumes are described in Section 3; we present scaling laws for the evolution of line plumes and describe various plume geometries under different parameters in Section 4; we derive scalings for the transit time in Sections 5 and 6 for two types of plume geometries, concentrated line plumes and well-mixed turbulence, respectively; Section 7 presents our conclusions.

## 2 METHODS

The ocean of Enceladus can be viewed as a layer of fluid confined between the seafloor and the ice shell, strongly influenced by rotation, and heated from below (Fig. 1A). Here, we neglect circulation induced by the interaction of the ocean with the ice above, but this is discussed in Kang & Flierl (2020), Lobo et al. (2021), Zhang, Kang & Marshall (2024), etc. We solve the Boussinesq equation:

$$\partial_t \mathbf{u} + \mathbf{u} \cdot \nabla \mathbf{u} + \mathbf{f} \times \mathbf{u} = -\nabla P + b\hat{\mathbf{z}} + \nu \nabla^2 \mathbf{u}, \quad (3)$$

$$\nabla \cdot \mathbf{u} = 0, \quad (4)$$

$$\partial_t T + \mathbf{u} \cdot \nabla T = \kappa \nabla^2 T, \quad (5)$$

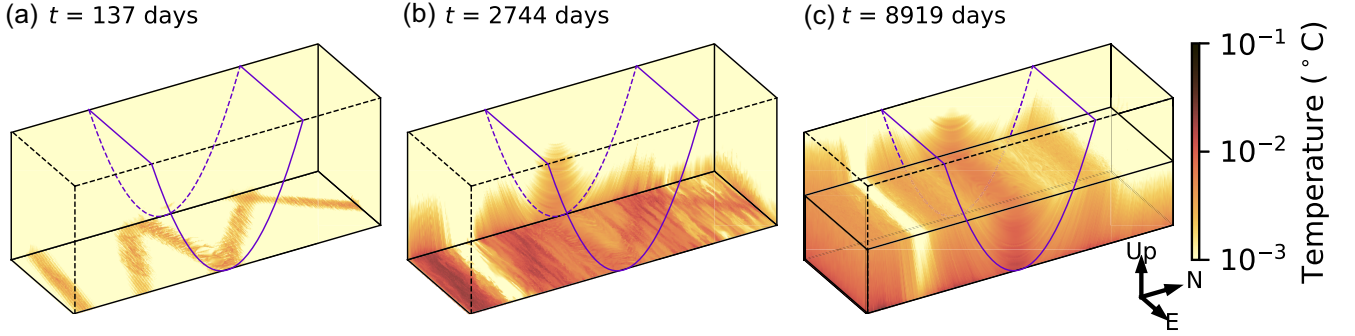


**Figure 2.** Plume evolution in the reference near-global simulation. The box in each panel is the domain of the simulation as in Fig. 1(B). Panels (A) and (B) show the longitude–latitude temperature pattern at the seafloor, while Panel (C) shows that for the middle depth. The plumes initially grow from the bottom heat sources but quickly become well-mixed before reaching the ocean top, especially in the zonal direction.

$$b = \alpha g(T - T_{\text{ref}}), \quad (6)$$

where  $\mathbf{u} = u\hat{x} + v\hat{y} + w\hat{z}$  is the three-component velocity;  $f$  is the Coriolis parameter;  $P$  is a scale field that represents pressure divided by the reference density;  $b$  is buoyancy  $b = -g\delta\rho/\rho_0$ , where  $\delta\rho$  is the density anomaly due to temperature perturbations;  $\nu$  and  $\kappa$  are viscosity and diffusivity;  $T$  is temperature and  $T_{\text{ref}} = 0^\circ\text{C}$  is the reference temperature;  $\alpha$  is thermal expansion coefficient. We prescribe a bottom heat flux and relax the temperature at the upper boundary to  $T_{\text{ref}} = 0^\circ\text{C}$ . The initial condition is one of no motion and a uniform temperature of  $T_{\text{ref}}$ .

We adopt a linear equation of state (equation 6), in which the thermal expansion coefficient  $\alpha$  is constant in each simulation. We consider two values of  $\alpha$ :  $1 \times 10^{-5} \text{ K}^{-1}$  and  $1.67 \times 10^{-4} \text{ K}^{-1}$  in different simulations (see Tables A1 and A2). The uncertainty in  $\alpha$  comes from the uncertainty of the mean salinity of the ocean in Enceladus. The ratio of  $\nu$  to  $\kappa$  (the Prandtl number  $\text{Pr}$ ) is set to unity in all our simulations.

We consider two domains: (1) near-global and (2) regional. Although the aforementioned parameters apply to both our near-global and regional simulations, there are differences in domain size, Coriolis parameter  $f$ , the bottom heat flux pattern, and diffusivity  $\nu$  as indicated below.

In our near-global simulations (Fig. 1B), a Cartesian coordinate system is used to represent the spherical geometry, as described in Bire et al. (2022) and Zhang et al. (2024). The domain is  $[0, L_x] \times [-\pi R, \pi R] \times [-H, 0]$  for  $(x, y, z)$ , where  $L_x = 50 \text{ km}$  is the zonal extent of the domain;  $R = 252 \text{ km}$  is the radius of Enceladus; and  $H$  is the depth of the ocean. The Coriolis parameter  $f$  follows the deep  $\beta$ -plane configuration (Grimshaw 1975; Dellar 2011):

$$\mathbf{f} = 2\Omega (\cos(y/R)\hat{y} + \sin(y/R)\hat{z}), \quad (7)$$

preserving the angle between  $\mathbf{f}$  and  $\mathbf{g}$ . In our reference near-global simulations, we concentrate the bottom heat flux along five randomly placed strips on the seafloor, in the spirit of Choblet et al. (2017) (Fig. 1B). This is the main difference between our near-global simulations and those of Bire et al. (2022). The global mean bottom heat flux in the reference simulation is  $1 \text{ W m}^{-2}$ . This results in a low Rossby number that is closest to a realistic value, although the real value for Enceladus is likely even lower. In addition to this reference near-global simulation, we perform additional simulations with different bottom heating values and patterns to test their effects on convection and associated transit time (Table A1). The four ‘stripy’ bottom heating patterns used in our study are shown in

Fig. A1. The diffusivity ( $\nu$ ) is set to  $2 \times 10^{-2} \text{ m s}^{-2}$  in all our near-global simulations.

In our regional simulations (Fig. 1C), the domain is a box of  $20 \text{ km} \times 20 \text{ km} \times 20 \text{ km}$ . We adopt an  $f$ -plane with  $\mathbf{f} = -2\Omega\hat{z}$  to represent the polar regions. We note that the goal of these regional simulation is not to capture the dynamics over the globe on Enceladus, which would require more realistic treatment of the geometry and plume pattern, but instead, our goal is to use this set of experiments to understand how plume morphology changes over time and to obtain scaling laws for transit time. Our regional simulations use an isotropic resolution of 40 meters, much higher than the 300 m resolution in our near-global simulations and Bire et al. (2022). In our reference simulation, we focus bottom heating over a single stripe (Fig. 3B1). We tested different bottom heating strengths and source widths and also performed a group of regional simulations with uniform bottom heating (Table A2). Diffusivity ( $\nu$ ) is  $1 \times 10^{-4} \text{ m s}^{-2}$  in our reference regional simulations: tests shows that sensitivity to  $\nu$  ( $\kappa$ ) is small in our simulations (Fig. A2).

We perform our simulations on GPUs using Oceananigans (Ramadhan et al. 2020). Spatial discretization uses a staggered Arakawa C-grid (Arakawa & Lamb 1977); the time integration is done with a 3rd-order Runge–Kutta method (Le & Moin 1991). We use a fifth-order WENO (weighted essentially non-oscillatory advection) scheme (Shu 2009) to calculate the advection terms in equations (3) and (5). A non-hydrostatic solver is used and a three-dimensional Fast Fourier Transform is employed to calculate  $P$  in equation (3).

To diagnose transport characteristics and, in particular, the bottom-to-top transit time, we release  $10^6$  passive neutrally buoyant Lagrangian particles in the regions where bottom heating is applied, similar to Bire et al. (2023). These particles follow the motion of the fluid, representing how passive tracers, such as chemicals and small particles, are transported by the fluid. By measuring when they reach the top of the ocean (defined as the top 10 per cent of the depth of the whole ocean), we get a distribution of the transit times. In most cases, we focus on the minimum transit time, which represents the likely fastest transport timescale. Later, we will see that even the minimum transit time is long compared to the chemical survival timescale of silicon particles assumed in Hsu et al. (2015; Section 6).

### 3 PHENOMENOLOGY OF REFERENCE SIMULATIONS

Although the bottom heating is focused along stripes, the plumes laterally mix well before reaching the mid-level of the ocean (Fig. 2). Fig. 2 shows the evolution of temperature. At time = 137 Earth days,

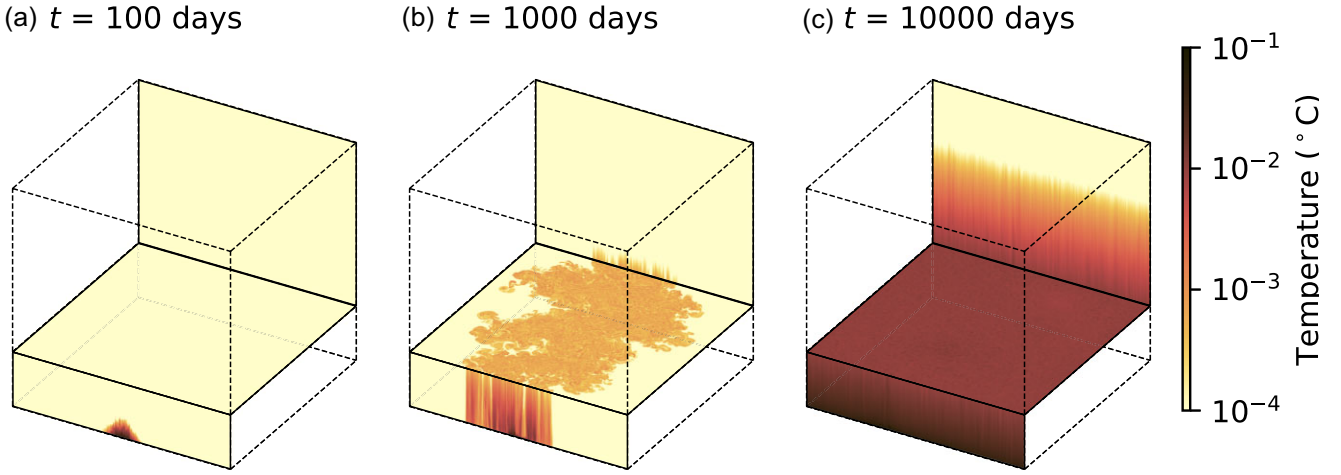


**Figure 3.** Plume evolution in the reference regional simulation. The box in each panel is the domain of the simulation as in Fig. 1(C). Panels (A, B, C) show the temperature distribution at several cross sections at different times. The horizontal cross section is set to 5 km above the seafloor. Since the domain is horizontally double periodic, the front and back walls refer to the same vertical cross section that is perpendicular to the bottom heating stripe. The plume driven by a line buoyancy source spreads horizontally and eventually becomes laterally well mixed due to baroclinic instability.

the warm plume water is still isolated and local to the heat sources (Fig. 2A). However, at time = 2744 Earth days, these initially isolated plumes merge into a large joint plume, (Fig. 2B) in which one cannot detect features of the prescribed bottom heating pattern (Fig. 2A) and (Fig. A1A). This merged plume continues to expand until it occupies the whole domain and becomes laterally well mixed (Fig. 2C). The evolution of the temperature profile in this simulation resembles that of passive tracers released on the seafloor Zeng & Jansen (2021), although they use uniform heating at the bottom. This shows that details of the bottom pattern are lost during vertical heat transmission.

The lateral mixing in our reference simulation (Fig. 2) is the combined effect of baroclinic instability (BCI) and the presence of zonal jets. In this simulation, the diffusivity  $\kappa$  is set to  $2 \times 10^{-2} \text{ m}^2 \text{ s}^{-1}$ , which implies a diffusive length scale ( $2\sqrt{\kappa t}$ ) of only 3 km at  $t = 2744$  d, far smaller than the width of the domain. This indicates that the strong lateral mixing observed here cannot be due to diffusion alone.

BCI occurs in the presence of horizontal temperature gradients. The temperature contrast between the centre of the plume and the ambient seawater provides the needed conditions. As a result of BCI, the buoyant water emanating from the plumes is mixed with the ambient denser water (Saunders 1973; Jones & Marshall 1993; Speer & Marshall 1995). Similar phenomena have been observed in laboratory experiments by Bush & Woods (1999) in which the evolution of a line plume is studied in both stratified and unstratified environments. The radius of the resulting vortices and the height of onset of BCI are reported to be  $(5.3 \pm 1.0)(B^{(\text{line})})^{1/3}/2\Omega$  and  $10(B^{(\text{line})})^{1/3}/2\Omega$ , respectively (Bush & Woods 1999). This will be tested further in our regional simulations in Section 4.1.

Under the influence of rotation, the kinetic energy generated by both convective and baroclinic instability cascades toward large scales and is eventually arrested by the  $\beta$ -effect at the Rhines scale, creating alternating zonal jets (Aurnou, Heimpel & Wicht 2007; Heimpel & Aurnou 2007; Ashkenazy & Tziperman 2021; Bire et al. 2022). These zonal jets further carry convective plumes downstream. Thus, it is easier for temperature anomalies to disperse in the zonal direction than in the meridional direction. This importance of the partitioning nature of zonal jets was also noted by Aurnou et al. (2007) and Lemasquerier, Bierson & Soderlund (2023).

Eddy-induced lateral mixing is also a dominant feature of our reference regional simulation (Fig. 3). Convection in this simulation is driven by bottom heating focused on a single stripe (Fig. 1C). Initially, the plume only develops where bottom heating is applied (Fig. 3A). Fast rim currents develop along the periphery of the line plume (Speer & Marshall 1995), which eventually leads to the split of the plume and the formation of multiple smaller circular plumes with weaker rim currents (Jones & Marshall 1993; Bush & Woods 1999; Goodman et al. 2004; Goodman & Lenferink 2012; Bire et al. 2023), during which a significant entrainment of cold ambient water occurs. The vortices formed from the instability scatter from the heat sources, transporting heat away. After hundreds of rotation periods, the plume becomes one order wider than the bottom heating stripe (Fig. 3B, C). Vortices can be seen in the  $x$ - $y$  plot of temperature at 5 km above the seafloor (Fig. 3B). Due to the small Rossby number, they are aligned with the rotational axis, forming Taylor columns (Bire et al. 2022; Kang et al. 2022). The flow patterns resemble a gas of vortices on an  $f$ -plane (Thompson & Young 2006; Gallet & Ferrari 2020). The plume eventually becomes laterally well mixed above 6 km. The  $x$ - $y$  view of temperature at 5 km above the seafloor shows almost no signature of the bottom heating pattern (Fig. 1C). Beyond this level, details of the bottom heating pattern will not play a role in transport efficiency.

By following Lagrangian particles, we find that the transit time exceeds 30 yr, 2 orders of magnitude greater than the prediction given by the free-fall scaling (Schoenfeld et al. 2023), but in line with the prediction given by Zeng & Jansen (2021) and Kang et al. (2022). It should be noted that, to compensate for limits in computational resources, this reference simulation uses a domain-averaged bottom heating of  $0.627 \text{ W m}^{-2}$ . This is at least one order of magnitude larger than the upper bound of the realistic value for Enceladus of  $0.04 \text{ W m}^{-2}$  (Čadek et al. 2016; Choblet et al. 2017). This means that the actual transit time on Enceladus is likely even longer. We will further discuss the scaling for the transit time in Section 6.

Our reference simulation motivates a simple model for plume evolution and a scaling for the transit time which is presented in Section 4. The plume evolution can be broken into two stages: an isolated line plume and laterally well mixed convective turbulence,



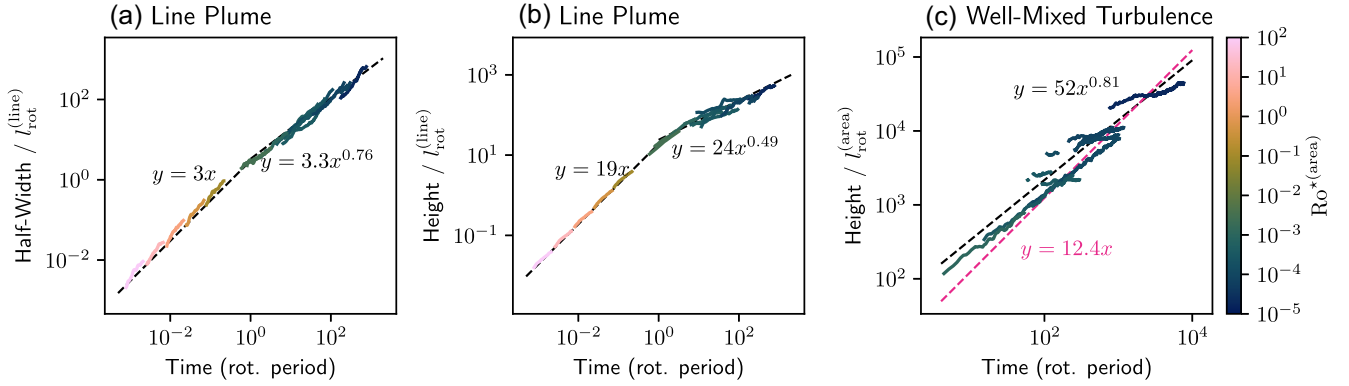


**Figure 4.** Development of line plumes and convective turbulence. Panels (A) and (B) show the half-width  $l$  and height  $h$  of a line plume normalized by  $l_{\text{rot}}^{(\text{line})}$  (equation 8) as a function of time in units of rotation periods; Panel (C) show the height of well-mixed convective turbulence normalized by  $h_{\text{rot}}^{(\text{area})}$  (equation 12) as a function of time in units of rotation periods. Black dashed lines are best fits, and the red dashed line in Panel (C) represents the scaling in Fernando et al. (1991). Each line represents one simulation (Table A2), and its color indicates the  $\text{Ro}^{*(\text{area})}$  of the corresponding simulation.

depending on whether the plume has reached the side boundaries or not. The former corresponds to Panels (A) and (B) of Fig. 3, while the latter corresponds to Panel (C). The mathematical descriptions of these two stages are given in Sections 4.1 and 6, respectively. Furthermore, both our regional and global simulations indicate that plumes on Enceladus will likely not remain concentrated because of mixing induced by BCI and zonal jets. This strong lateral mixing implies a long transit time from the seafloor to the ocean top with two processes at work. First, trajectories of particles are no longer straight upward as previously assumed but involve significant horizontal stochastic motion. Secondly, the details of the bottom heating are smoothed out, and thus the transit time depends more on the domain averaged bottom heating (smaller than  $0.04 \text{ W m}^{-2}$ ) than on the local maximum (several  $\text{W m}^{-2}$ ). Based on this, in Section 6, we propose a scaling law for transit time on Enceladus.

## 4 DOES THE PLUME ENVELOPE AND HEATING PATTERN PROJECT ONTO THE ICE SHELL?

### 4.1 Free line plume development in an infinite domain

The first stage of the reference regional simulation can be conceptualized as a line plume along the strip of bottom heating. We seek to express the evolution of the half-width  $l$  and height  $h$  of the plume as a function of the controlling parameters and time  $t$ , after the plume has progressed far enough to neglect the finite width of the bottom source, but before it undergoes instability or encounters the upper or lateral boundaries. In this case, we may describe the bottom heating as a geometric line, from which emanates a buoyancy flux  $B^{(\text{line})}$  (in units of  $\text{m}^3 \text{ s}^{-3}$ ), and the domain can be viewed as infinite.

The key physical parameters in the system are the buoyancy flux line density  $B^{(\text{line})}$  and the background rotation rate  $\Omega$ . Combining these two parameters gives us the only length scale in the system

$$l_{\text{rot}}^{(\text{line})} = \frac{(B^{(\text{line})})^{\frac{1}{3}}}{2\Omega}, \quad (8)$$

which is known as a rotational length scale (Jones & Marshall 1993; Speer & Marshall 1995; Bire et al. 2022). The Coriolis force begins to dominate the evolution of the plume at a height of order  $10l_{\text{rot}}^{(\text{line})}$  (Bush & Woods 1999).

Dimensional analysis requires that  $l$  (or  $h$ ), when normalized by  $l_{\text{rot}}^{(\text{line})}$ , be a function of non-dimensional time  $\tilde{t}$ :

$$l/l_{\text{rot}}^{(\text{line})} = \tilde{l}(\tilde{t}), \quad h/l_{\text{rot}}^{(\text{line})} = \tilde{h}(\tilde{t}) \quad (9)$$

where  $\tilde{t}$  is the number of rotation periods:  $\Omega t/(2\pi)$ .

In Fig. 4(A, B), we plot  $l/l_{\text{rot}}^{(\text{line})}$  and  $h/l_{\text{rot}}^{(\text{line})}$  from our regional simulations against  $\tilde{t}$ . These simulations use various bottom heating strengths, background rotation rates, and domain sizes (Table A2). Data from simulations with different rotation rates and heat fluxes overlap with each other, supporting our dimensional analysis. We construct empirical laws for  $\tilde{l}(\tilde{t})$  and  $\tilde{h}(\tilde{t})$  using log-log linear regressions to obtain power laws [the black dashed lines in Fig. 4(A, B)].

It takes several rotation periods for the Coriolis force to influence the flow. Up until that time, the plume behaves as if the fluid were not rotating (Jones & Marshall 1993; Maxworthy & Narimousa 1994). Thus, during this developing stage  $l$  and  $h$  are expected to depend on  $B^{(\text{line})}$  and  $t$  but not on  $\Omega$ . Writing out equation (9):  $l = (B^{(\text{line})})^{\frac{1}{3}}(2\Omega)^{-1}\tilde{l}(\Omega t/2\pi)$ , we find  $\tilde{l}$  must be a linear function to ensure that  $\Omega$  cancels out. For the same reason,  $\tilde{h}$  must also be a linear function. This prediction is tested against our simulations in Fig. 4(A,B) which shows the half-width  $l$  and height  $h$  of the line plume plotted as a function of non-dimensional time  $\tilde{t}$ . Fitting the data with power laws gives exponents of  $0.97 \pm 0.02$  and  $0.98 \pm 0.02$  (where  $\pm$  indicates one sigma uncertainty) for  $l$  and  $h$ , respectively. The plume height and width, both linear functions of time, implies that the aspect ratio of the plume does not change over time. This is consistent with the wedge-shaped non-rotating line plume in the classic model which has a half angle of  $(6/5)\alpha$ , where  $\alpha$  is the entrainment coefficient (Morton, Taylor & Turner 1956).

When  $\tilde{t} > 1$ , rotation begins to play a role. The half-width of the plume  $l$  grows faster than the plume height  $h$  (Fig. 4A,B). The fitted dependence of  $\tilde{l}$  and  $\tilde{h}$  on  $\tilde{t}$  has exponents of  $0.76 \pm 0.04$  and  $0.49 \pm 0.05$  (one sigma), respectively. It is evident that  $l/h$  increases with time, as follows  $\tilde{t}^{0.3}$ . This agrees with the plume evolution of the reference simulation (Fig. 3), in which the plume reaches the side boundaries before the ocean top. The faster growth of  $l$  compared to  $h$  is likely due to BCI, which generates vertically aligned vortices with large horizontal velocities. Similar phenomena also occur in point plumes in fast-rotating environments: the plume height stops growing after the onset of BCI, while the plume width starts to increase (Goodman & Lenferink 2012; Bire et al. 2023).

#### 4.2 Four possible plume geometries in a finite domain

The geometry of the plumes in a finite domain depends on two key non-dimensional numbers: the natural Rossby number  $Ro^{*(line)} \equiv l_{rot}^{(line)}/H$  (equation 1) and the aspect ratio  $\Gamma$  defined as

$$\Gamma \equiv L/H. \quad (10)$$

$Ro^{*(line)}$  determines whether the plume will be influenced by rotation and whether BCI occurs or not (Goodman et al. 2004; Bire et al. 2022);  $\Gamma$  controls whether the line plume reaches the ocean top or side boundaries first. Since our regional simulations use doubly periodic boundary conditions,  $L$  actually represents the distance between the bottom heating stripes under periodic extensions. For realistic icy moons like Enceladus,  $L$  is a measure for the sparseness of bottom heating features.

Comparing the key heights and widths of a free line plume with the domain height and width, we can determine the geometry of the plume when it reaches the upper surface. In the non-dimensional parameter space spanned by  $Ro^{*(line)}$  and  $\Gamma$ , we identify 4 different regimes, depending on whether the plume reaches the side or top boundary first and whether the rotational effects dominates eventually. The former is demarcated by the black curve, while the latter is demarcated by the red curve in Fig. 5. The complete derivation is given in Appendix A. The characteristic of these regimes are:

(i) **Non-rotating line plume.** With large  $Ro^{*(line)}$  and large  $\Gamma$  (the upper right corner of Fig. 5), the plume is wedge shaped as in the classic model of non-rotating plumes, a consequence of the entrainment of ambient water into the plume (Morton et al. 1956). This behaviour indicates that the bottom heating pattern cannot be exactly projected onto the ocean top even for very strong bottom heating because of the inevitable presence of entrainment.

(ii) **Non-rotating well-mixed turbulence.** With large  $Ro^{*(line)}$  and small  $\Gamma$  (the lower right corner of Fig. 5), the wedge-shaped plume reaches the lateral boundaries first. The plume then mixes vertically and also becomes horizontally well-mixed. Eventually, the plume becomes similar to that driven by uniform bottom heating.

(iii) **Fast-rotating line plume.** With small  $Ro^{*(line)}$  and large  $\Gamma$  (the upper middle sector Fig. 5), the plume is strongly influenced by the Coriolis effect in the early stage, and thus is no longer wedge-shaped. Numerical simulations for point plumes in the ocean of Europa by Goodman & Lenferink (2012) fall into this regime (green shading in Fig. 5, further discussed in Section 7), and qualitative similar behaviour has been found in them. After reaching the ocean top, the line plume undergoes BCI and splits the plume into vortices, transporting heat away from the source.

(iv) **Fast-rotating well-mixed turbulence.** For small  $Ro^{*(line)}$  and small  $\Gamma$  (the lower left corner of Fig. 5), the initial development is similar to the previous rotating line-plume regime. The plume undergoes BCI and transports heat away from the source, filling the entire horizontal domain. Thereafter, the temperature pattern becomes horizontally well mixed, and the dynamics resemble those forced by uniform bottom heating. This regime will be discussed in Section 6.

#### 5 TRANSIT TIME FOR CONCENTRATED LINE PLUMES (REGIME I, III)

In this section, we will derive the scaling law for the transit time for the scenario where the line plume is not laterally well-mixed by the time it reaches the top boundary [regimes (i) and (iii) of Fig. 5]. As elaborated in Section 4.1, the development of a line plume should be

governed by the integrated buoyancy flux  $B^{(line)}$  (in units of  $m^3 s^{-3}$ ), the background rotation  $\Omega$ , and the ocean depth  $H$ . Following this, we presented a general form of how the plume height  $h$  evolves over time (equation 9 and Fig. 4B). The transit time can thus be estimated as the time it takes for the plume height  $h$  reaching the ocean depth  $H$ . Substituting  $h = H = l_{rot}^{(line)}/Ro^{*(line)}$  into equation (9) and using the fitted power-law relations in Fig. 4(B), we get the transit time in units of rotation periods as a function of  $Ro^{*(line)}$ :

$$\Omega \tau_{transit}^{(line)}/2\pi = \begin{cases} (19Ro^{*(line)})^{-1} & (Ro^{*(line)} \geq 0.033) \\ (24Ro^{*(line)})^{-\frac{1}{0.39}} & (Ro^{*(line)} \leq 0.033). \end{cases} \quad (11)$$

Here,  $Ro^{*(line)} = 0.033$  corresponds to the transition point from a non-rotating line plume to a rotating line plume [regime (i) in Fig. 5; Morton et al. 1956]. In the non-rotating regime (regime i,  $Ro^{*(line)} \geq 0.033$ ), we can show that the expression for  $\tau_{transit}^{(line)}$  does not depend on  $\Omega$ , using the definition of  $Ro^{*(line)}$  given by equation (1):

$$\tau_{transit}^{(line)} \sim H/B^{(line)}^{\frac{1}{3}}.$$

In the fast-rotating regime (regime iii,  $Ro^{*(line)} \geq 0.033$ ), the Coriolis force starts to influence the fluid motion and then the baroclinic instability will cause the line plume to spread (Bush & Woods 1999). As a result,  $\tau_{transit}^{(line)}$  increases quickly with decreased  $Ro^{*(line)}$  following a power law of an exponents of roughly  $-2$ , informed by our simulations. We collect all our regional simulations (Table A2) using a line bottom heat source, we diagnose the time at which the plumes reaches a certain height, and we present the diagnosed transit time in Fig. 6(A). We make sure that all these diagnostics are conducted before the plume becomes homogenized laterally. All our simulations agree well with the transit time scaling given by equation (11) (Fig. 6A).

Bouffard et al. (2025) conducted similar simulations to constrain the convection transit time, forced by a bottom heating concentrated along a line Choblet et al. (2017). Using the rms speed  $U_{rms}$  presented in the table 1 of Bouffard et al. (2025), we estimated the transit time following  $D/U_{rms}$ , and we overlaid their results in Fig. 6(A) as a function of  $Ro^{*(line)}$ . To obtain  $Ro^{*(line)}$  for their experiments, we need to know the integrated buoyancy flux  $B^{(line)}$ . This is calculated by dividing the total heat flux backed out of their modified flux-based Rayleigh number  $Ra_{qj}$  and Ekman number  $E$ , over the length of the meridian. As can be seen from Fig. 6(A), the dependence of transit time on  $Ro^{*(line)}$  is in generally in agreement with our scaling laws. The transit time from Bouffard et al. (2025) is longer than ours with similar  $Ro^{*(line)}$  by almost a constant factor, because we diagnosed the fastest transit time whereas they estimated the average value. Since neither their simulations nor ours can reach the parameter regime relevant for Enceladus, extrapolation is thus needed. Because the two works found different scaling laws, the transit time for Enceladus given by Bouffard et al. (2025) differs by 3–4 orders of magnitude compared to our scaling. This discrepancy stems from the extrapolation which is over many orders of magnitude following a slightly different scaling law and a larger thermal expansion coefficient ( $\alpha_T = 3.6 \times 10^{-4} K^{-1}$ ) assumed in Bouffard et al. (2025).

#### 6 TRANSIT TIME IN THE WELL-MIXED REGIME (REGIME II, IV)

If the domain is tall enough for the plume to fall in the ‘fast rotating well-mixed turbulence’ regime (Fig. 3C), the plume undergoes instability, which then leads to lateral homogenization of the heat flux. Beyond the level of homogenization, the detailed pattern of

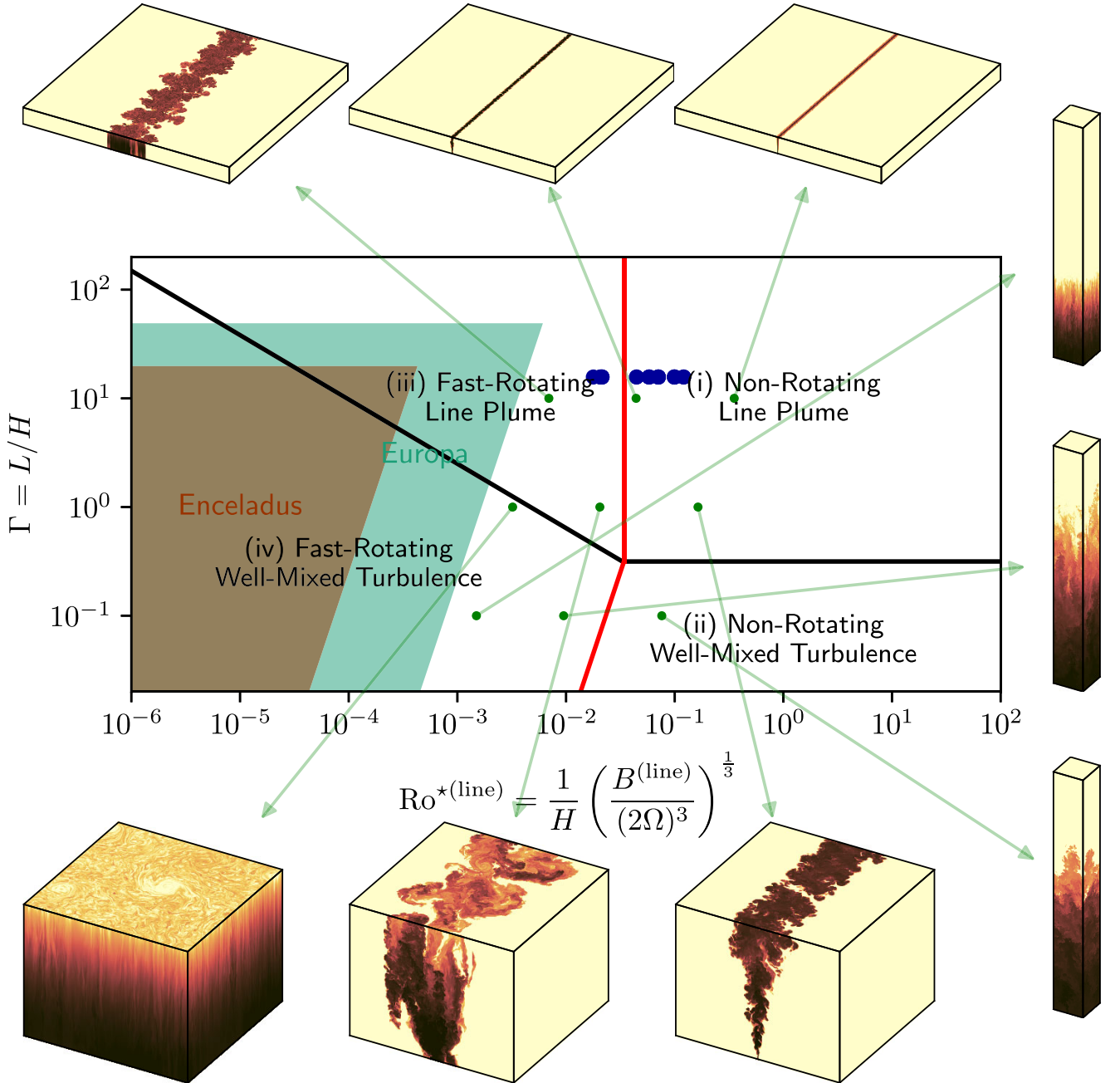


**Figure 5.** Plume geometries for given key non-dimensional numbers. The  $x$ - and  $y$ -axes represent the natural Rossby number  $Ro^{*(line)}$  (equation 1) and the domain aspect ratio  $\Gamma$  (equation 10), respectively. Depending on whether the plume reaches the side or top boundary first (the black curve) and whether the plume is dominated by the Coriolis force (the red curve), the parameter space is divided into 4 regimes. The temperature distributions in 9 of our simulations are shown here with the same colour map as in Fig. 3) to illustrate the plume envelope in different regimes. Likely parameter ranges for Enceladus are shown by the shading in the lower left corner:  $Ro^{*(line)} \leq 4 \times 10^{-4}$  and  $\Gamma \leq 20$ , as discussed in Section 7. The green shading represents the possible parameter ranges for Europa:  $Ro^{*(line)} \leq 5 \times 10^{-3}$  and  $\Gamma \leq 50$ . The right side of the parameter space of Enceladus (and Europa) is tilted because both  $Ro^{*(line)}$  and  $\Gamma$  depends on the domain size  $L$  for a given total heating flux (see Section 7). Dark blue dots represent simulations by Bouffard et al. (2025, discussed in Section 6). Bouffard et al. (2025) simulated convection driven by the bottom heating pattern in Choblet et al. (2017) with various bottom heating strengths to allow deriving a scaling for the transit time. The presented  $Ro^{*(line)}$  of these simulations is calculated from the total buoyancy inferred from their modified flux-based Rayleigh number  $Ra_q$ .

heat flux at the bottom no longer influences the dynamics and transport. Instead, the domain-averaged buoyancy flux  $B^{(area)}$  (in units of  $m^2 s^{-3}$ ) and the background rotating rate  $\Omega$  become the key parameters that govern the transport efficiency. In this section, we consider the convective transit time forced by a uniform bottom heat flux.

Similar to equation (8), we define a rotation length scale following (Fernando et al. 1991; Bire et al. 2022):

$$l_{rot}^{(area)} = \left( \frac{B^{(area)}}{(2\Omega)^3} \right)^{\frac{1}{2}}. \quad (12)$$

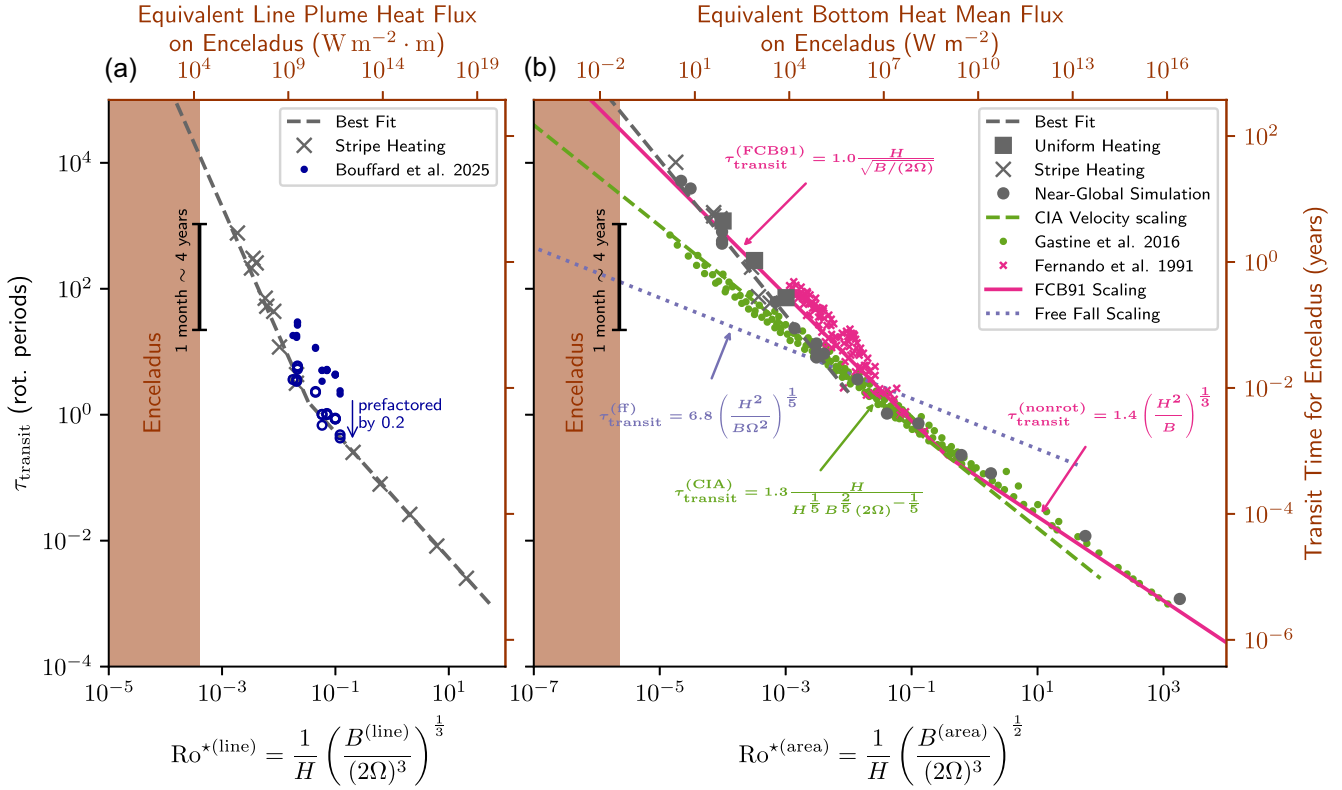


**Figure 6.** Transit time in units of rotation periods plotted against the natural Rossby number. For regimes (i, non-rotating line plume) and (iii, fast-rotating line plume), the transit time is plotted against  $Ro^{*(line)}$  (equation 1) in Panel A. The best fit (dashed grey line) follows equation (11). Dark blue dots represent spherical shell convection simulations by Bouffard et al. (2025), discussed in Section 5, and dark blue empty circles represent the transit time pre-factored by 0.2, since Bouffard et al. (2025) report the mean transit time while we consider fastest transit. The upper x-axis shows the corresponding heat flux (equation 1). Note that the unit of heat flux here is  $W m^{-1}$ , which is roughly the characteristics heat flux times the stripe width. For regimes (ii, non-rotating well-mixed turbulence) and (iv, fast-rotating well-mixed turbulence), the transit time is plotted against  $Ro^{*(area)}$  (equation 2) in Panel (B). Our regional simulations (grey squares for uniform bottom heating; grey crosses for heating focused over a stripe) and near-global simulations (grey dots) broadly agree with the scaling derived from the best fit (equation 14) of the turbulence height evolution (Fig. 4C) and the FCB91 scaling (equation 13) by Fernando et al. (1991). Red crosses show lab experiments in fig. 18 of Fernando et al. (1991). The green dashed line and dots indicate the inferred transit time from the characteristic velocity in the CIA scaling (Aurnou et al. 2020) and numerical simulations by Gastine, Wicht & Aubert (2016). The purple dotted line shows the free-fall velocity scaling (Schoenfeld et al. 2023). Panels (A) and (B) share y-axes. The upper x-axis shows the corresponding heat flux (equation 2). All other parameters are the same as Section 1 expect for the varying heat flux. The shading indicates the likely parameter regime for Enceladus: the implied transit time will be tens or hundreds of years according to our best fit or the FCB91 scaling. On each panel, the transit time proposed by Hsu et al. (2015) of ‘months to several years’ is marked by a black error bar between 1 month to 4 years.

Note that the ratio of  $l_{rot}^{(area)}$  and  $H$  defines the area-averaged natural Rossby number  $Ro^{*(area)}$  (equation 2; Jones & Marshall 1993; Maxworthy & Narimousa 1994).

In Fernando et al. (1991) (hereafter FCB91), it has been hypothesized that the plume height  $H$  should grow at the characteristic velocity of convective turbulence:  $u_{rot}^{(area)} \equiv (B/2\Omega)^{1/2}$  (Aurnou et al. 2020; Bire et al. 2022). In their lab experiments, the height of convective turbulence follows  $h \approx 0.7(B^{(area)}\Omega^{-3})^{1/2}\Omega t$ , which yields a transit time in units of rotation periods for a given height  $H$ :

$$\Omega\tau_{transit}^{(FCB91)}/2\pi = 0.08 Ro^{*(area)-1} \quad (13)$$

This is broadly consistent with our simulations (Fig. 4C), although the least square regression yields an exponent of  $0.81 \pm 0.09$  (one sigma), instead of 1. Using our best fit (black line and equation in Fig. 4C), the formula for the transit time in units of rotation periods is

$$\Omega\tau_{transit}^{(fit)}/2\pi = 0.0078 Ro^{*(area)-1.23}. \quad (14)$$

The above two scalings are plotted in Fig. 6(B). For the small  $Ro^{*(area)}$  on Enceladus, for example,  $1 \times 10^{-6}$ , the relative difference between  $\tau_{transit}^{(FCB91)}$  and  $\tau_{transit}^{(fit)}$  is approximately a factor of 2, while both have an order of  $10^5$  rotation periods.

When the domain is too shallow for the plume to be influenced by rotation ( $Ro^{*(area)} > 1$ ), the height of the plume follows  $h \approx 0.3(B^{(area)}t^3)^{1/2}$  (Fernando, Boyer & Chen 1989). Replacing  $h$  with  $H$  and  $t$  with  $\tau_{transit}$ , we obtain the formula for the transit time for non-rotating well-mixed turbulence:

$$\tau_{transit}^{(nonrot)} = 1.4 H^{2/3} B^{-1/3}. \quad (15)$$

After multiplying both sides of equation (15) by  $\Omega/2\pi$ , the left hand side becomes the non-dimensional transit time, while the right hand side becomes  $0.11 Ro^{*(area)2/3}$ . This relation suggests plotting  $\tau_{transit}^{(nonrot)}$  in Fig. 6(B), even though  $\Omega$  is a redundant parameter in this non-rotating regime.

In Fig. 6(B), we also overlay the transit time diagnosed from our regional and near-global simulations (grey dots, crosses, and squares) and the lab results from FCB91 (red crosses). They all generally agree



with our scaling predictions, regardless of the different domain sizes and bottom heating patterns.

We may infer the transit time from previous studies on Rayleigh–Bénard convection with rotation (Gastine et al. 2016; Plumley & Julien 2019) by considering the timescale of  $H/U$ , where  $U$  is the characteristic velocity. Gastine et al. (2016) performed 227 rotating convection simulations in a spherical shell forced by buoyancy contrast. The Nusselt number (total heat flux divided by diffusive heat flux) and Reynolds number (mean r.m.s velocity normalized by  $\nu/H$ ) in all simulations are tabulated in their appendix, enabling us to calculate  $Ro^{*(area)}$  (equation 2) and inferred transit time  $H/U$ . The simulations in Gastine et al. (2016) with  $Nu > 2$  are plotted as green dots in Fig. 6. Additionally, we can derive a scaling for  $H/U$  using the CIA (balance between Coriolis-inertial-Archimedean forces) scaling for velocity (Aurnou et al. 2020):

$$\Omega \tau_{transit}^{(CIA)} / 2\pi = 0.1 Ro^{*(area)}^{-\frac{4}{5}}. \quad (16)$$

The coefficient of 0.1 is chosen to match Gastine et al. (2016). This relation is plotted as the green dashed line in Fig. 6(B). It is no surprise that the inferred transit time in the study of Gastine et al. (2016) matches well with equation (16), because both stem from the characteristic velocity in the fast-rotating diffusivity-free regime rather than the transit time. We notice that simulations by Gastine et al. (2016) and the CIA velocity scaling suggest a slightly shorter transit time than found in our simulations and the scaling by FCB91 (equation 13). This might be due to the fact that  $H/U$  is actually a lower bound for  $\tau_{transit}$ , since the motion of particles can be stochastic. The convective scale  $l$  scales with  $(Ro^{*(area)})^{\frac{2}{3}} H$  in the fast rotation regime but is equal to  $H$  in the non-rotating limit (Aurnou et al. 2020). This may also explain why simulations with large  $Ro^{*(area)}$  in Gastine et al. (2016) agree well with  $\tau_{transit}^{(nonrot)}$  scaling (equation 15).

In our scaling, we have assumed that the dynamics on icy satellites are highly supercritical and have already reached the diffusive-less regime, which requires that viscosity ( $\nu$ ) and diffusivity ( $\kappa$ ) do not influence the plume evolution (Section 4.1) and the transit time (Section 6). To test this assumption, we performed a group of simulations in which we varied the viscosity and diffusivity, while keeping the Prandtl number at unity. The tested values are  $1 \times 10^{-4}$ ,  $1 \times 10^{-3}$ ,  $1 \times 10^{-2}$ , and  $1 \times 10^{-1} \text{ m}^2 \text{ s}^{-1}$ , and the first value corresponds to our reference simulation (presented in Section 3).

Our tests show a very weak sensitivity to viscosity (diffusivity) if values are below  $10^{-3} \text{ m}^2 \text{ s}^{-1}$  (Fig. A2). In our first two simulations (Fig. A2A, B), in which  $\nu = 1 \times 10^{-4}$  and  $1 \times 10^{-3} \text{ m}^2 \text{ s}^{-1}$ , the horizontal temperature distributions at 5 km above the seafloor show eddy-dominant features, implying that the lateral mixing is mostly due to eddies generated from baroclinic eddies. The vortices under  $\nu = 1 \times 10^{-3} \text{ m}^2 \text{ s}^{-1}$  have slightly larger sizes, likely due to small-scale turbulence being damped. The plume heights are almost identical in these two simulations. The plume width under  $\nu = 1 \times 10^{-4} \text{ m}^2 \text{ s}^{-1}$  is roughly 20 per cent greater than that under  $\nu = 1 \times 10^{-3} \text{ m}^2 \text{ s}^{-1}$ . In our other two simulations (Fig. A2C, D), in which  $\nu = 1 \times 10^{-2}$  and  $1 \times 10^{-1} \text{ m}^2 \text{ s}^{-1}$ , the temperature patterns are close to the purely diffusive solution, implying that eddies are suppressed by the large diffusivity.

## 7 DISCUSSION AND APPLICATIONS TO ENCELADUS

Using both numerical simulations and scaling analysis, we have arrived at the following conclusions.

(i) Rotating line plumes are susceptible to baroclinic instability, which results in efficient lateral mixing. When focusing 30 GW of heating along a median circle, the plume will expand laterally to a half-width of 70 km due to entrainment of ambient water when reaching the ocean top (regime (iii) in Fig. 5). For even smaller  $Ro^{*(line)}$  (equation (1)) and the geometrical aspect ratio  $\Gamma$  (equation (10)), combined with homogenization by alternating zonal jets, small-scale details of bottom heating are efficiently mixed away in the ocean interior and are unlikely to be projected onto the ocean top [regime (iv) in Fig. 5].

(ii) After the plume structure associated with the heating pattern is disrupted by baroclinic instability, the tracer transit time is governed by (1) the integrated heat flux over the stripe for regime (iii) or (2) zonal-mean or global-mean bottom heat flux for regime (iv) rather than the peak heat flux.

(iii) Scaling for transit time is proposed and tested against numerical simulations and previous laboratory experiments for all our four parameter regimes. Extrapolating this scaling to parameters appropriate to the ocean of Enceladus, we conclude that the transit time there is likely many decades.

It has been proposed by Choblet et al. (2017) that the bottom heating on Enceladus may be concentrated along stripes rather than evenly distributed, as a result of convective circulation within the porous core. This motivates this work to consider the dynamics of a line plume. When the tidal dissipation in the core is polar amplified, the bottom heating tends to be concentrated along a single meridian, whereas when the tidal dissipation is evenly distributed, the bottom heating pattern resembles a spider web (Choblet et al. 2017). Both polar amplified (Choblet et al. 2017; Liao, Nimmo & Neufeld 2020; Rovira-Navarro et al. 2022) and equatorward amplified (Rovira-Navarro et al. 2022) tidal dissipation in the core may be realized depending on the rheology and transmissivity of the core. Furthermore, while existing models yield dissipated power in the ice shell that is much smaller than the present-day heat loss, the amount of dissipation that can be generated remains unclear due to the significant uncertainty associated with ice rheology and viscosity (Robuchon et al. 2010; Běhounková et al. 2013; Shoji et al. 2013; Beuthe 2019; Souček et al. 2019); moreover, it is unclear whether today’s Enceladus is in an equilibrium state (Goldreich, Lithwick & Luan 2025). As shown by Goldreich et al. (2025), if Enceladus happens to be in a low eccentricity state during a limit cycle oscillation, the total heat production within Enceladus could be as low as 2 GW, 30 times lower than the heat needed to balance the present-day conductive heat loss. All these factors cast uncertainty over the amplitude and distribution of the bottom heating.

To make predictions for Enceladus, we need to estimate the non-dimensional numbers –  $Ro^{*(line)}$  and  $\Gamma$  [and  $Ro^{*(area)}$  for regimes (ii) and (iv)]. The upper limit of  $Ro^{*(line)}$  is derived by assuming all 30 GW of heating is generated in the core and injected into the ocean along a single meridian, which is  $1.6 \times 10^3 \text{ km}$  long for Enceladus. This gives us a line density of heat of  $Q^{(line)} = 1.9 \times 10^4 \text{ W m}^{-1}$ . If the peak heat flux is  $10 \text{ W m}^{-2}$  following Choblet et al. (2017), the width of the heating stripe should be 2 km. Substituting  $\alpha = 1 \times 10^{-5} \text{ K}^{-1}$ ,  $\rho_0 = 1.02 \times 10^3 \text{ kg m}^{-3}$ ,  $c_p = 4 \times 10^3 \text{ J kg}^{-1} \text{ K}^{-1}$  (Soderlund 2019),  $\Omega = 5.3 \times 10^{-5} \text{ s}^{-1}$ ,  $g = 0.1 \text{ m s}^{-2}$  and  $H = 40 \text{ km}$  (Čadež et al. 2016; Tajeddine et al. 2017; Hemingway & Mittal 2019; McKinnon & Schenk 2021), we get the upper limit of Enceladean  $Ro^{*(line)}$  using equation (1):

$$Ro^{*(line)} \leq 4 \times 10^{-4}. \quad (17)$$

The upper bound of  $\Gamma \equiv H/L$  (equation 10) can be obtained by setting  $L$  (the distances between bottom heating stripes) to  $\pi R$ , where  $R$  is the radius of Enceladus, with  $H = 40$  km being the ocean depth, yielding

$$\Gamma \leq 10. \quad (18)$$

We highlight the plausible range of  $Ro^{*(line)}$  and  $\Gamma$  in Fig. 5. Note that  $\Gamma$  and  $Ro^{*(line)}$  are not independent of each other to ensure a constant total heat production rate does not exceed 30 GW, i.e.  $4\pi R^2(Q^{(line)}/L) = 30$  GW. This interconnection causes the right-side boundary of the Enceladus parameter regime to be tilted. For a given value of  $Q^{(area)}$ , the maximum possible value of  $Q^{(line)}$  also depends on  $\Gamma$ , since a decrease in  $\Gamma$  is due to an increase in the number of bottom heating stripes, which makes  $B^{(line)}$  and therefore  $Ro^{*(line)}$  smaller.

As can be seen from Fig. 5, the Enceladean ocean is likely to reside in regime (iii, fast-rotating line plume) and regime (iv, fast-rotating well-mixed turbulence). If in regime (iv), the strong lateral mixing will smooth out details of bottom heating, the global-mean heat (buoyancy) flux, represented by  $Ro^{*(area)}$ , is more relevant to the transit time estimation (equations 13, 14, and 16). Spreading 30 GW of heating over the seafloor, we get a mean heat flux of  $Q^{(area)} = 0.04 \text{ W m}^{-2}$ . Using the same  $\alpha$ ,  $\rho_0$ ,  $c_p$ ,  $\Omega$ ,  $g$ , and  $H$  as we estimate the range of  $Ro^{*(line)}$  (equation 17), following the definition by equation (2), we obtain a range of  $Ro^{*(area)}$  on Enceladus:

$$Ro^{*(area)} \leq 2 \times 10^{-6}. \quad (19)$$

Following the discussion in Section 6, the transit time  $\tau_{\text{transit}}$  is roughly inversely proportional to  $Ro^{*(area)}$  (equations 13 and 14). This predicts a transit timescale longer than  $4 \times 10^4$  rotation periods, which corresponds to at least one hundred years in real time. Even if we assume a heat flux of  $\sim 500 \text{ mW m}^{-2}$ , the transit time is as long as 30 yr. Furthermore, the stratification induced by either negative thermal expansion coefficient in a fresh ocean (Melosh et al. 2004; Zeng & Jansen 2021; Kang et al. 2022; Bire et al. 2023) or by the lateral temperature/salinity gradient beneath the ice (Lobo et al. 2021; Kang & Jansen 2022; Zhang et al. 2024) can prolong the transit time to at least one hundred years (Zeng & Jansen 2021; Ames et al. 2025).

If the total power generated in the core to be equal to 35 GW and all this bottom heating is focused over at most three bottom heating stripes, Enceladus can also reside in regime (iii, fast-rotating line plume). In this regime, lateral mixing due to baroclinic instability still causes considerable lateral spreading of the plume, although it is not strong enough to completely homogenize the upward heat flux. Our model for the line plume envelope evolution (equation 9 and Fig. 4) predicts that, if heat is concentrated along a single meridian as suggested by Choblet et al. (2017), the half-width of the line plume will be 71 km after propagating through a 40 km deep ocean. The transit time  $\tau_{\text{transit}}^{(line)}$ , in turn, can be estimated to be greater than  $1.3 \times 10^4$  rotation periods (50 Earth years) following equation (11) and Fig. 6(A).

Irrespective of whether Enceladus is in regime (iii) or regime (iv), the transit time is found to be much greater than the transit time proposed by Hsu et al. (2015) of ‘months to several years’ (marked by the black error bar in Fig. 6 as 1 month  $\sim 4$  yr). Moreover, as can be seen from our near-global simulations (Section 3), the alternating zonal jets formed in the presence of  $\beta$ -effect facilitate further mixing along the zonal direction. This makes it even more difficult to keep the line plume focused on Enceladus, and the transit time is expected to be longer because the upward buoyancy flux becomes even more ‘diluted’.

We may estimate the transit time on Europa following the same approach, assuming that the heat from Europa core is also concentrated along stripes. Similar to Enceladus, we estimated the upper bounds for  $Ro^{*(line)}$  and  $Ro^{*(area)}$ , considering an extreme scenario, where a bottom heating of  $1 \times 10^3$  GW (Běhounková et al. 2021) is focused along a single meridian. Assuming  $\alpha = 3 \times 10^{-4} \text{ K}^{-1}$ , (Soderlund 2019; Bire et al. 2023),  $\Omega = 2.1 \times 10^{-5} \text{ s}^{-1}$ ,  $g = 1.3 \text{ m s}^{-2}$ ,  $R = 1.56 \times 10^3$  km and  $H = 1 \times 10^2$  km (Hand, Carlson & Chyba 2007; Soderlund et al. 2014), we obtain the parameter regime for Europa as highlighted by green shading in Fig. 5. Again, both regimes (iii, fast-rotating line plume) and (iv, fast-rotating well-mixed turbulence) are relevant for Europa. Since the maximum possible value of  $Ro^{*(line)}$  and  $Ro^{*(area)}$  due to the much greater thermal expansion coefficient and gravitational acceleration compared to Enceladus, convective plumes undergo less lateral spreading caused by baroclinic instability and have much short transit time ( $\sim 70$  rotation periods) on Europa. The relative unimportance of baroclinic instability and short transit times agrees with previous simulations for convection plumes on Europa driven by point heating sources (Goodman et al. 2004; Goodman & Lenferink 2012; Bire et al. 2023).

## ACKNOWLEDGEMENTS

This project uses Oceananigans, an open source ocean general circulation model. The authors thank Simone Silvestri, Gregory L. Wagner, and Xin Kai Lee for technical support for Oceananigans and Tucker Ely, Chris German, Kaushal Gianchandni for helpful discussion. This work was supported in part by NASA Astrobiology Grant 80NSSC19K1427 ‘Exploring Ocean Worlds’.

## DATA AVAILABILITY

The data used in this article are available on Zenodo: <https://doi.org/10.5281/zenodo.15668410>.

## REFERENCES

- Abramov O., Spencer J. R., 2009, *Icarus*, 199, 189
- Ames F., Ferreira D., Czaja A., Masters A., 2025, *Commun. Earth Environ.*, 6, 63
- Arakawa A., Lamb V. R., 1977, *Gen. Circ. Models Atmos.*, 17, 173 <https://doi.org/10.1016/B978-0-12-460817-7.50009-4>
- Ashkenazy Y., Tziperman E., 2021, *Nat. Commun.*, 12, 1 <https://doi.org/10.1038/s41467-021-26710-0>
- Aurnou J., Andreadis S., Zhu L., Olson P., 2003, *Earth Planet. Sci. Lett.*, 212, 119
- Aurnou J., Heimpel M., Wicht J., 2007, *Icarus*, 190, 110
- Aurnou J. M., Horn S., Julien K., 2020, *Phys. Rev. Res.*, 2, 043115
- Běhounková M., Tobie G., Choblet G., Čadež O., 2013, *Icarus*, 226, 898
- Běhounková M., Tobie G., Choblet G., Kervazo M., Melwani Daswani M., Dumoulin C., Vance S. D., 2021, *Geophys. Res. Lett.*, 48, e2020GL090077
- Beuthe M., 2016, *Icarus*, 280, 278
- Beuthe M., 2018, *Icarus*, 302, 145 <https://doi.org/10.1038/s41550-017-0289-8>
- Beuthe M., 2019, *Icarus*, 332, 66
- Bire S., Kang W., Ramadhan A., Campin J.-M., Marshall J., 2022, 127, *J. Geophys. Res.: Planets*, e2021JE007025
- Bire S., Mittal T., Kang W., Ramadhan A., Tuckman P. J., German C. R., Thurnherr A. M., Marshall J., 2023, *J. Geophys. Res.: Planets*, 128, e2023JE007740
- Bouffard M., Choblet G., Amit H., Tobie G., Čadež O., Terra-Nova F., 2025, *Nat. Astron.*, 9, 1
- Bush J. W., Woods A. W., 1999, *J. Fluid Mech.*, 388, 289

Čadek O. et al., 2016, *Geophys. Res. Lett.*, 43, 5653 <https://doi.org/10.1002/2016GL068634>

Choblet G., Tobie G., Sotin C., Běhounková M., Čadek O., Postberg F., Souček O., 2017, *Nat. Astron.*, 1, 841

Christensen U. R., Aubert J., 2006, *Geophys. J. Int.*, 166, 97

Collins G., Head III J., Pappalardo R., Spaun N., 2000, *J. Geophys. Res.: Planets*, 105, 1709

Dellar P. J., 2011, *J. Fluid Mech.*, 674, 174

Ermakov A. I. et al., 2021, *Planet. Sci. J.*, 2, 157

Fernando H. J., Boyer D. L., Chen R.-R., 1989, *Dynamics Atmos. Oceans*, 13, 95

Fernando H. J., Chen R.-R., Boyer D. L., 1991, *J. Fluid Mech.*, 228, 513

Gallet B., Ferrari R., 2020, *Proc. Nat. Acad. Sci.*, 117, 4491

Gastine T., Wicht J., Aubert J., 2016, *JFM*, 808, 690

Goldreich P., Lithwick Y., Luan J., 2020, preprint ([arXiv:2503.01967](https://arxiv.org/abs/2503.01967))

Goodman J. C., Lenferink E., 2012, *Icarus*, 221, 970

Goodman J. C., Collins G. C., Marshall J., Pierrehumbert R. T., 2004, *J. Geophys. Res.: Planets*, 109

Grimshaw R. H. J., 1975, *Tellus*, 27, 351

Hand K. P., Carlson R. W., Chyba C. F., 2007, *Astrobiol.*, 7, 1006

Heimpel M., Aurnou J., 2007, *Icarus*, 187, 540 <https://doi.org/10.1016/j.icarus.2006.10.023>

Hemingway D. J., Mittal T., 2019, *Icarus*, 332, 111

Hsu H.-W. et al., 2015, *Nature*, 519, 207

Jess L. et al., 2014, *Science*, 344, 78 <https://doi.org/10.1126/science.1250551>

Jones H., Marshall J., 1993, *J. Phys. Oceanogr.*, 23, 1009

Kang W., Flierl G., 2020, *Proc. Nat. Acad. Sci.*, 117, 14764

Kang W., Jansen M., 2022, *Astrophys. J.*, 935, 103

Kang W., Marshall J., Mittal T., Bire S., 2022, *MNRAS*, 517, 3485

Le H., Moin P., 1991, *J. Comput. Phys.*, 92, 369

Lemasquerier D. G., Bierson C. J., Soderlund K. M., 2023, *AGU Adv.*, 4, e2023AV000994

Liao Y., Nimmo F., Neufeld J. A., 2020, *J. Geophys. Res.: Planets*, 125, e2019JE006209

Lobo A. H., Thompson A. F., Vance S. D., Tharimena S., 2021, *Nat. Geosci.*, 14, 185

Maxworthy T., Narimousa S., 1994, *J. Phys. Oceanogr.*, 24, 865

McKinnon W., Schenk P., 2021, in AGU Fall Meeting Abstracts. p. P35C, <https://ui.adsabs.harvard.edu/abs/2021AGUFM.P35C2141M>

Melosh H., Ekholm A., Showman A., Lorenz R., 2004, *Icarus*, 168, 498

Morton B. R., Taylor G. I., Turner J. S., 1956, *Proc. R. Soc. A*, 234, 1

Nimmo F., Neveu M., Howett C., 2023, *Space Sci. Rev.*, 219, 57

Plumley M., Julien K., 2019, *Earth Space Sci.*, 6, 1580

Porco C. C. et al., 2006, *Science*, 311, 1393

Postberg F., Kempf S., Schmidt J., Brilliantov N., Beinsen A., Abel B., Buck U., Srama R., 2009, *Nature*, 459, 1098 <https://doi.org/10.1038/nature08046>

Postberg F. et al., 2018, *Nature*, 558, 564

Ramadhan A. et al., 2020, *J. Open Source Softw.*, 5, 2018

Robuchon G., Choblet G., Tobie G., Čadek O., Sotin C., Grasset O., 2010, *Icarus*, 207, 959

Rovira-Navarro M., Katz R. F., Liao Y., van der Wal W., Nimmo F., 2022, *J. Geophys. Res.: Planets*, 127, e2021JE007117

Saunders P. M., 1973, *J. Phys. Oceanogr.*, 3, 61

Schoenfeld A. M., Hawkins E. K., Soderlund K. M., Vance S. D., Leonard E., Yin A., 2023, *Commun. Earth Environ.*, 4, 28

Sekine Y. et al., 2015, *Nat. Commun.*, 6, 8604

Shoji D., Hussmann H., Kurita K., Sohl F., 2013, *Icarus*, 226, 10

Shu C.-W., 2009, *SIAM Rev.*, 51, 82 <https://doi.org/10.1137/070679065>

Silvestri S., Wagner G. L., Campin J.-M., Constantinou N. C., Hill C. N., Souza A., Ferrari R., 2024, *J. Adv. Model. Earth Sys.*, 16, e2023MS004130

Soderlund K. M., 2019, *Geophys. Res. Lett.*, 46, 8700

Soderlund K., Schmidt B., Wicht J., Blankenship D., 2014, *Nat. Geosci.*, 7, 16 <https://doi.org/10.1038/ngeo2021>

Souček O., Běhounková M., Čadek O., Hron J., Tobie G., Choblet G., 2019, *Icarus*, 328, 218

Speer K. G., Marshall J., 1995, *J. Marine Res.*, 53, 1025

Tajeddine R., Soderlund K. M., Thomas P. C., Helfenstein P., Hedman M. M., Burns J. A., Schenk P. M., 2017, *Icarus*, 295, 46 <https://doi.org/10.1016/j.icarus.2017.04.019>

Taubner R.-S. et al., 2018, *Nat. Commun.*, 9, 1

Thomas P., Tajeddine R., Tiscareno M., Burns J., Joseph J., Loredó T., Helfenstein P., Porco C., 2016, *Icarus*, 264, 37 <https://doi.org/10.1016/j.icarus.2015.08.037>

Thompson A. F., Young W. R., 2006, *J. Phys. Oceanogr.*, 36, 720

Thomson R. E., Delaney J. R., 2001, *J. Geophys. Res.: Planets*, 106, 12355

Turner J., 1969, *Annu. Rev. Fluid Mech.*, 1, 29

Vance S., Goodman J., 2009, in Pappalardo R. T., McKinnon W. B., Khurana K., eds, Europa. University of Arizona Press, Tucson, p. 459

Waite J. H. et al., 2006, *Science*, 311, 1419

Zeng Y., Jansen M. F., 2021, *Planet. Sci. J.*, 2, 151 <https://doi.org/10.3847/PSJ/ac1114>

Zhang Y., Kang W., Marshall J., 2024, *Sci. Adv.*, 10, eadn6857

## APPENDIX A: DERIVATION FOR OUR REGIME DIAGRAM

The height and half-width of a line plume increase over time at different rates (Fig. 4). We consider a critical case in which the lateral and top boundaries are reached at the same time. We set  $l = L/2$  and  $h = H$  in equation (9):

$$\frac{L/2}{l_{\text{rot}}^{(\text{line})}} = \tilde{l}(\tilde{t}), \quad \frac{H}{l_{\text{rot}}^{(\text{line})}} = \tilde{h}(\tilde{t}) \quad (\text{A1})$$

where  $\tilde{t}$  is the number of rotation periods. From equation (A1), we derive a parametric curve for  $(\text{Ro}^{(\text{line})}, \Gamma)$  using  $\tilde{t}$  as the parameter:

$$\text{Ro}^{(\text{line})} = \frac{1}{\tilde{h}(\tilde{t})}, \quad \Gamma = \frac{2\tilde{l}(\tilde{t})}{\tilde{h}(\tilde{t})}. \quad (\text{A2})$$

For the non-rotating regime ( $\tilde{t} \ll 1$ ), the line plume follows:

$$\tilde{l} \approx 3\tilde{t}, \quad (\text{A3})$$

$$\tilde{h} \approx 19\tilde{t}. \quad (\text{A4})$$

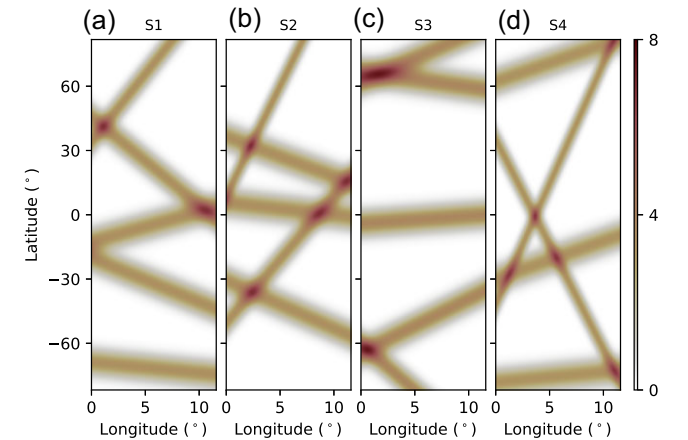


**Figure A1.** Bottom heat flux patterns used in our near-global simulations. The values plotted in Panels (A), (B), (C), and (D) are normalized by the global-mean value of each simulation, and the actual heat flux patterns should be multiplied by  $Q^{(\text{area})}$  listed in Table A1. Our reference near-global simulation (Fig. 2) uses S1 (Panel A, here).

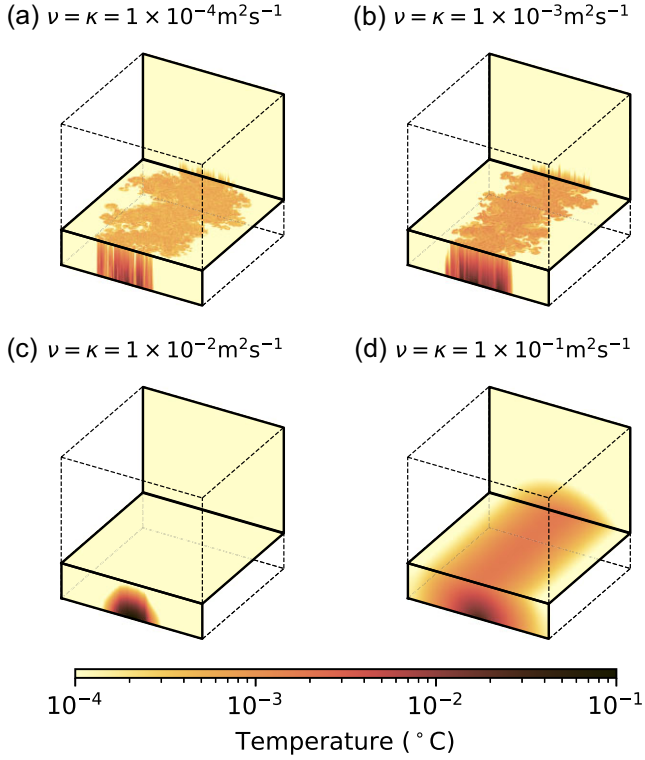


**Figure A2.** Sensitivity tests for viscosity and diffusivity. Panels (A, B, C, D) show the temperature distribution at 1000 Earth days in four simulations with various viscosity and diffusivity. The Prandtl number is unity here. The bottom heating is the same in these four simulations, and the first simulation (Panel A) is our reference simulation. The first two simulations (Panels A, B) are dominated by eddies, and the plume heights and widths are almost the same, implying very weak sensitivity to viscosity and diffusivity. The last two simulations (Panels C, D) show diffusion-dominant distributions of temperature, and eddies are suppressed.

We may eliminate  $\tilde{t}$  from equation (A2), which gives:

$$\Gamma \approx 0.3. \quad (\text{A5})$$

For the fast-rotating regime ( $\tilde{t} > 1$ ), the line plume follows:

$$\tilde{t} \approx 3.3\tilde{t}^{0.76}, \quad (\text{A6})$$

**Table A1.** Near-global simulations.

$H$ (km)	$\Omega$ (s <sup>-1</sup> )	$Q^{(\text{area})}$ (W m <sup>-2</sup> )	$Q$ Distribution	$\text{Ro}^{*(\text{area})}$	Figs.
60	$5.3 \times 10^{-5}$	$1 \times 10^0$	S1	$3.09 \times 10^{-5}$	2,6
60	$5.3 \times 10^{-5}$	$1 \times 10^1$	S2	$9.77 \times 10^{-5}$	6
60	$5.3 \times 10^{-5}$	$1 \times 10^4$	S2	$3.09 \times 10^{-3}$	6
60	$5.3 \times 10^{-5}$	$1 \times 10^1$	S3	$9.77 \times 10^{-5}$	6
60	$5.3 \times 10^{-5}$	$1 \times 10^4$	S3	$3.09 \times 10^{-3}$	6
60	$5.3 \times 10^{-5}$	$5 \times 10^{-1}$	S4	$2.18 \times 10^{-5}$	6
60	$5.3 \times 10^{-5}$	$1 \times 10^1$	Uniform	$9.77 \times 10^{-5}$	6
60	$5.3 \times 10^{-5}$	$5 \times 10^2$	Uniform	$6.91 \times 10^{-4}$	6
30	$5.3 \times 10^{-5}$	$5 \times 10^2$	Uniform	$1.38 \times 10^{-3}$	6
60	$5.3 \times 10^{-5}$	$1 \times 10^4$	Uniform	$3.09 \times 10^{-3}$	6
10	$5.3 \times 10^{-5}$	$5 \times 10^2$	Uniform	$4.06 \times 10^{-3}$	6
30	$5.3 \times 10^{-5}$	$5 \times 10^4$	Uniform	$1.38 \times 10^{-2}$	6
10	$5.3 \times 10^{-5}$	$5 \times 10^4$	Uniform	$4.06 \times 10^{-2}$	6
10	$5.3 \times 10^{-5}$	$5 \times 10^5$	Uniform	$1.29 \times 10^{-1}$	6
30	$5.3 \times 10^{-6}$	$1 \times 10^5$	Uniform	$6.18 \times 10^{-1}$	6
10	$5.3 \times 10^{-6}$	$1 \times 10^5$	Uniform	$1.82 \times 10^0$	6
10	$5.3 \times 10^{-7}$	$1 \times 10^5$	Uniform	$5.75 \times 10^1$	6
10	$5.3 \times 10^{-8}$	$1 \times 10^5$	Uniform	$1.82 \times 10^3$	6

*Note.* This table shows the ocean depth ( $H$ ), rotation rate of the moon ( $\Omega$ ), global-mean bottom flux ( $Q^{(\text{area})}$ ), distribution of bottom flux, natural Rossby number ( $\text{Ro}^{*(\text{area})}$ ), and figures that use this simulation (the 'Figs' column). In all our near-global simulations, viscosity (along with diffusivity) is  $2 \times 10^{-2} \text{ m}^2 \text{ s}^{-1}$  and the thermal expansion coefficient is  $1.67 \times 10^{-4} \text{ K}^{-1}$ . For the bottom heating distribution, S1, S2, S3, and S4 represents different bottom heating patterns shown in Fig. A1.

$$\tilde{h} \approx 24\tilde{t}^{0.49}. \quad (\text{A7})$$

Then, equation (A2) becomes

$$\Gamma \approx 0.05 (\text{Ro}^{*(\text{line})})^{-0.55} \quad (\text{A8})$$

Equations (A5) and (A8) combine to form the black curve in Fig. 5. The intersection between equations (A5) and (A8) is at  $\text{Ro}^{*(\text{line})} \approx 0.04$ .  $\text{Ro}^{*(\text{line})}$  and  $\text{Ro}^{*(\text{area})}$  determine the transition between the non-rotating and fast-rotating regimes when reaching the top boundary for line plumes and well-mixed turbulence, respectively. Thus, the red curve in Fig. 5 comprises a constant line for  $\text{Ro}^{*(\text{line})} \approx 0.033$  above the black curve and another line for  $\text{Ro}^{*(\text{area})} \approx 0.07$  below the black curve.



Table A2. Regional simulations.

$L$ (kilometer)	$\Omega$ ( $s^{-1}$ )	$\alpha$ ( $K^{-1}$ )	$\nu$ ( $m^2 s^{-1}$ )	$D$ (meter)	$Q^{(max)}$ ( $W m^{-2}$ )	$Q^{(line)}$ ( $W m^{-1}$ )	$Ro^{(line)}$	$Q^{(area)}$ ( $W m^{-2}$ )	$Ro^{(area)}$	Figs
20	$5.30 \times 10^{-5}$	$1.00 \times 10^{-5}$	$1 \times 10^{-4}$	$5.0 \times 10^2$	$1.0 \times 10^1$	$1.3 \times 10^4$	$6.9 \times 10^{-4}$	$6.3 \times 10^{-1}$	$1.8 \times 10^{-5}$	3,4,6A,6B
20	$2.12 \times 10^{-4}$	$1.67 \times 10^{-4}$	0	$8.0 \times 10^1$	$2.5 \times 10^4$	$5.0 \times 10^6$	$3.2 \times 10^{-3}$	$2.5 \times 10^2$	$1.8 \times 10^{-4}$	4,5
20	$5.30 \times 10^{-5}$	$1.67 \times 10^{-4}$	0	$8.0 \times 10^1$	$1.0 \times 10^5$	$2.0 \times 10^7$	$2.0 \times 10^{-2}$	$1.0 \times 10^3$	$2.9 \times 10^{-3}$	4,5,6A
2	$2.12 \times 10^{-4}$	$1.67 \times 10^{-4}$	0	$8.0 \times 10^1$	$2.5 \times 10^3$	$5.0 \times 10^5$	$1.5 \times 10^{-3}$	$2.5 \times 10^2$	$1.8 \times 10^{-4}$	5
200	$2.12 \times 10^{-4}$	$1.67 \times 10^{-4}$	0	$8.0 \times 10^1$	$2.5 \times 10^5$	$5.0 \times 10^7$	$6.9 \times 10^{-3}$	$2.5 \times 10^2$	$1.8 \times 10^{-4}$	5,6A
2	$5.30 \times 10^{-5}$	$1.67 \times 10^{-4}$	0	$8.0 \times 10^1$	$1.0 \times 10^4$	$2.0 \times 10^6$	$9.5 \times 10^{-3}$	$1.0 \times 10^3$	$2.9 \times 10^{-3}$	5
200	$5.30 \times 10^{-5}$	$1.67 \times 10^{-4}$	0	$8.0 \times 10^1$	$1.0 \times 10^6$	$2.0 \times 10^8$	$4.4 \times 10^{-2}$	$1.0 \times 10^3$	$2.9 \times 10^{-3}$	5,6A
2	$6.63 \times 10^{-6}$	$1.67 \times 10^{-4}$	0	$8.0 \times 10^1$	$1.0 \times 10^4$	$2.0 \times 10^6$	$7.6 \times 10^{-2}$	$1.0 \times 10^3$	$6.6 \times 10^{-2}$	5
20	$6.63 \times 10^{-6}$	$1.67 \times 10^{-4}$	0	$8.0 \times 10^1$	$1.0 \times 10^5$	$2.0 \times 10^7$	$1.6 \times 10^{-1}$	$1.0 \times 10^3$	$6.6 \times 10^{-2}$	5
200	$6.63 \times 10^{-6}$	$1.67 \times 10^{-4}$	0	$8.0 \times 10^1$	$1.0 \times 10^6$	$2.0 \times 10^8$	$3.5 \times 10^{-1}$	$1.0 \times 10^3$	$6.6 \times 10^{-2}$	5,6A
20	$5.30 \times 10^{-5}$	$1.00 \times 10^{-5}$	$1 \times 10^{-4}$	—	—	—	—	$2.0 \times 10^1$	$1.0 \times 10^{-4}$	4,6B
20	$5.30 \times 10^{-5}$	$1.00 \times 10^{-5}$	$1 \times 10^{-4}$	—	—	—	—	$2.0 \times 10^2$	$3.2 \times 10^{-4}$	4,6B
20	$5.30 \times 10^{-5}$	$1.00 \times 10^{-5}$	$1 \times 10^{-4}$	—	—	—	—	$2.0 \times 10^3$	$1.0 \times 10^{-3}$	4,6B
20	$5.30 \times 10^{-5}$	$1.00 \times 10^{-5}$	$1 \times 10^{-4}$	$5.0 \times 10^2$	$1.6 \times 10^2$	$2.0 \times 10^5$	$1.7 \times 10^{-3}$	$1.0 \times 10^1$	$7.2 \times 10^{-5}$	4,6A,6B
20	$5.30 \times 10^{-5}$	$1.00 \times 10^{-5}$	$1 \times 10^{-4}$	$2.0 \times 10^3$	$4.0 \times 10^1$	$2.0 \times 10^5$	$1.7 \times 10^{-3}$	$1.0 \times 10^1$	$7.2 \times 10^{-5}$	4,6A,6B
20	$5.30 \times 10^{-5}$	$1.00 \times 10^{-5}$	$1 \times 10^{-4}$	$2.0 \times 10^3$	$6.4 \times 10^1$	$3.2 \times 10^5$	$2.0 \times 10^{-3}$	$1.6 \times 10^1$	$9.1 \times 10^{-5}$	4,6A,6B
20	$5.30 \times 10^{-5}$	$1.00 \times 10^{-5}$	$1 \times 10^{-4}$	$5.0 \times 10^2$	$2.6 \times 10^3$	$3.2 \times 10^6$	$4.4 \times 10^{-3}$	$1.6 \times 10^2$	$2.9 \times 10^{-4}$	4,6A,6B
20	$2.65 \times 10^{-5}$	$1.67 \times 10^{-4}$	0	$8.0 \times 10^1$	$2.0 \times 10^2$	$4.0 \times 10^4$	$5.2 \times 10^{-3}$	$2.0 \times 10^0$	$3.7 \times 10^{-4}$	4,6A,6B
20	$5.30 \times 10^{-5}$	$1.00 \times 10^{-5}$	$1 \times 10^{-4}$	$5.0 \times 10^2$	$1.0 \times 10^4$	$1.3 \times 10^7$	$6.9 \times 10^{-3}$	$6.3 \times 10^2$	$5.7 \times 10^{-4}$	4,6A,6B
20	$5.30 \times 10^{-5}$	$1.00 \times 10^{-5}$	$1 \times 10^{-4}$	—	—	—	—	$1.0 \times 10^0$	$2.3 \times 10^{-5}$	4
20	$5.30 \times 10^{-5}$	$1.67 \times 10^{-4}$	0	$8.0 \times 10^1$	$2.0 \times 10^2$	$4.0 \times 10^4$	$2.6 \times 10^{-3}$	$2.0 \times 10^0$	$1.3 \times 10^{-4}$	4
20	$1.33 \times 10^{-5}$	$1.67 \times 10^{-4}$	0	$8.0 \times 10^1$	$2.0 \times 10^2$	$4.0 \times 10^4$	$1.0 \times 10^{-2}$	$2.0 \times 10^0$	$1.0 \times 10^{-3}$	4,6A
20	$6.63 \times 10^{-6}$	$1.67 \times 10^{-4}$	0	$8.0 \times 10^1$	$2.0 \times 10^2$	$4.0 \times 10^4$	$2.1 \times 10^{-2}$	$2.0 \times 10^0$	$3.0 \times 10^{-3}$	4,6A
20	$5.30 \times 10^{-6}$	$1.67 \times 10^{-4}$	0	$8.0 \times 10^1$	$1.0 \times 10^5$	$2.0 \times 10^7$	$2.0 \times 10^{-1}$	$1.0 \times 10^3$	$9.3 \times 10^{-2}$	4,6A
20	$1.77 \times 10^{-6}$	$1.67 \times 10^{-4}$	0	$8.0 \times 10^1$	$1.0 \times 10^5$	$2.0 \times 10^7$	$6.1 \times 10^{-1}$	$1.0 \times 10^3$	$4.8 \times 10^{-1}$	4,6A
20	$5.30 \times 10^{-7}$	$1.67 \times 10^{-4}$	0	$8.0 \times 10^1$	$1.0 \times 10^5$	$2.0 \times 10^7$	$2.0 \times 10^0$	$1.0 \times 10^3$	$2.9 \times 10^0$	4,6A
20	$1.77 \times 10^{-7}$	$1.67 \times 10^{-4}$	0	$8.0 \times 10^1$	$1.0 \times 10^5$	$2.0 \times 10^7$	$6.1 \times 10^0$	$1.0 \times 10^3$	$1.5 \times 10^1$	4,6A
20	$5.30 \times 10^{-8}$	$1.67 \times 10^{-4}$	0	$8.0 \times 10^1$	$1.0 \times 10^5$	$2.0 \times 10^7$	$2.0 \times 10^1$	$1.0 \times 10^3$	$9.3 \times 10^1$	4,6A

Note. This table shows the domain size in the  $x$  and  $y$  directions ( $L$ ), the rotation rate of the moon ( $\Omega$ ), thermal expansion coefficient ( $\alpha$ ), viscosity ( $\nu$ ), peak heating ( $Q^{(max)}$ ) and 'width' ( $D$ , standard deviation) of the Gaussian bottom heat pattern, integrated line density of heat flux ( $Q^{(line)}$ ), natural Rossby number for line plumes ( $Ro^{(line)}$ ), domain-averaged heat flux ( $Q^{(area)}$ ), natural Rossby number for domain-averaged buoyancy flux ( $Ro^{(area)}$ ), and figures that uses that simulation (the 'Figs' column). The four simulations use uniform bottom heating, and thus  $D$ ,  $Q^{(max)}$ ,  $Q^{(line)}$ , and  $Ro^{(line)}$  are not shown for them. The Prandtl number is unity in all simulations, meaning that diffusivity ( $\kappa$ ) is equal to viscosity ( $\nu$ ). The usage of a WENO scheme (Shu 2009; Silvestri et al. 2024) ensures numerical stability under zero viscosity. The grid size, which is the same in  $x$ ,  $y$ , and  $z$  directions, is 20, 40, and 200 meters for  $L$  of 2, 20, and 200 kilometers, respectively.

This paper has been typeset from a  $\text{\LaTeX}$  file prepared by the author.